Check for updates

Cellulose nanofiber-scaffolded rGO/WO₃ membrane for photocatalytic degradation of methylene blue under visible light irradiation†

Medhanit Tefera Yifira,[abc] Gebrehiwot Gebreslassie, [ID] [abd] Anteneh Kindu Mersha [ID] *[abe] and Kebede Nigussie Mekonnen [ID] *[ab]

Although membrane-based water treatment has advanced significantly and many commercial products are currently available, its practical application remains limited, particularly in regions with inadequate electricity infrastructure. In this study, cellulose-based photocatalytic membranes incorporating visible light-active rGO/WO₃ nanoparticles into a cellulose nanofiber (CNF) scaffold were fabricated using a simple casting method. The structure–property relationships of the nanostructures and the membranes were examined, and the membranes were tested for the photocatalytic degradation of methylene blue (MB). The CNF/rGO/WO₃ composite membrane demonstrated significantly higher photodegradation capacity (89.3%) compared to pure WO₃ (50.13%) for MB under visible light, with consistent performance for up to ten cycles. After ten cycles of repeated use, the membrane retained a degradation efficiency of 48%, which is comparable to that of WO₃. This notable performance was attributed to improved charge separation, enhanced visible light absorption, larger surface area, and synergistic interactions among the components within the composite membrane. Besides enhancing photodegradation capacity through increased charge carrier separation, CNF played a vital role in immobilizing and stabilizing the photocatalyst. The principal active species identified in the photocatalytic material include h+, $^{\bullet}O_2^-$, and $^{\bullet}OH$, with a slight predominance of h^+. The simplicity of cellulose-mediated, visible-light active functional membrane design and fabrication creates opportunities for low-cost solutions to address water and energy challenges in environments with limited infrastructure. These visible light-responsive membrane materials hold great promise for applications in areas such as food packaging, surface disinfection, and the development of self-healing materials.

ᵃDepartment of Industrial Chemistry, Addis Ababa Science and Technology University, P.O. Box 16417, Addis Ababa, Ethiopia. E-mail: antenhen.kindu@aastu.edu.et; kebede.nigussie@aastu.edu.et

ᵇNanotechnology Centers of Excellence, Addis Ababa Science and Technology University, P.O. Box 16417, Addis Ababa, Ethiopia

ᶜDepartments of Chemistry, Wolkite University, P.O. Box 07, Wolkite, Ethiopia

ᵈSchool of Mechanical and Electrical Engineering, University of Electronic Science and Technology of China, Chengdu 611731, China

ᵉInstitute for Nanotechnology and Water Sustainability, College of Engineering, Science and Technology, University of South Africa, Florida Science Campus, Roodepoort 1709, South Africa

† Electronic supplementary information (ESI) available. See DOI: https://doi.org/10.1039/d5ra03227j

Introduction

Water pollution has emerged as a significant global environmental issue.[1] It has become a worldwide environmental and public health concern, as the majority of areas across the world are facing a shortage of freshwater.[2] Industrial discharges, including heavy metal ions and textile dyes, are among the primary contributors to water pollution.[3] Many organic pollutants, such as textile dyes, exhibit high toxicity, and their high chemical stability and poor biodegradability lead to environmental persistence. Moreover, organic dye such as methylene blue (MB) is difficult to treat with traditional physicochemical or biochemical methods. Higher concentrations of organic dyes are associated with different health effects such as discoloration of urine, vomiting, tissue necrosis, abdominal pain, hypertension, and anemia.[3] This calls for the development of efficient methods for remediating organic dyes in industrial effluents.

Water treatment methods such as membrane filtration[4] and the use of ion exchange membranes[5] and adsorption[6–8] have been studied to reclaim dye-contaminated water. However, in addition to process inefficiency, these techniques involve the transition of contaminants from their liquid to solid states, creating secondary pollutants that could potentially harm the environment and complicate process technology.[9] Photocatalysis, on the other hand, is recognized as a highly effective and promising technology because it can successfully remove organic pollutants from water without creating hazardous byproducts.[10] Due to its unique qualities, such as cost-effectiveness, process simplicity, and response to visible light, photocatalytic technologies are advancing rapidly in the wastewater treatment industry.[9]

Semiconductor materials use solar energy to drive chemical reactions, creating electron–hole pairs. This process includes the formation of highly reactive species, such as hydroxyl radicals ($^{\bullet}OH$) and superoxide radicals ($^{\bullet}O_2^-$), following a sequence of oxidation and reduction events. They serve as the primary oxidizing agents for the conversion of organic dyes into green products.[11] Tungsten trioxide (WO_3) is widely utilized as a semiconductor photocatalyst and it provides one of the most effective means to degrade organic dyes from water because it is a versatile metal oxide with outstanding chemical stability and good film-forming and coating properties.[12] However, limitations such as its absorption in only the UV region, the rapid recombination of photogenerated electron/hole (e^-/h^+) pairs, easy agglomeration, difficulty of recycling, and high energy costs, restrict its large-scale applications.[13]

To improve the photocatalytic properties of WO_3 and, more importantly, facilitate the recycling and reuse of the catalyst, it is essential to load WO_3 onto substrates such as reduced graphene oxide (rGO), molecular sieves, and natural minerals.[14] Such substrate materials not only bind WO_3 particles but also serve as excellent electron mediators to adjust electron transfer and improve electron–hole separation by restraining the recombination of photogenerated charges. These substrates also enhance the visible light absorption capacity of WO_3.[15] For example, Dhivyaprasath et al.[16] incorporated WO_3 into a rGO/WO_3 composite thin film with 88% MB degradation performance after 120 min irradiation. Zhu et al.[15] utilized rGO/WO_3 composites for the removal of 98% sulfonamide under visible light irradiation. However, although these powdered composite materials exhibit excellent performance in pollutant degradation, recovering the photocatalyst from the treated wastewater and reusing it in further treatment cycles is challenging.[15,17]

Immobilizing photocatalysts such as rGO/WO_3 nanocomposites in filtration membranes produce photocatalytic membranes (PCMs) that allow both photodegradation and catalyst recovery. This, in turn, imparts self-cleaning properties to the membrane, further increasing the lifetime of the photocatalyst and overall treatment performance. This class of membranes also minimizes biofouling, a critical challenge in membrane separation.[2] Several researchers have reported photocatalytic nanocomposite membranes for water treatment applications, such as PVDF-MoS_2/WO_3-PVA membrane,[17] rGO/TiO_2-PPSU hybrid ultrafiltration membranes,[18] CNF/ZnO–Ag membrane,[19] and CNF/Ag_2/Se composite films.[20] In the present work, a cellulose nanofiber (CNF) scaffolded rGO/WO_3 nanocomposite membrane was developed and tested for photodegradation of MB dye. The CNF-networks provide a platform for uniform distribution of rGO/WO_3 nanomaterials,[21] resulting in high surface area, improved stability of the resulting nanocomposite, and decreased electron–hole recombination rate, making CNF an ideal carrier for rGO/WO_3 nanoparticles.

Materials and methods

Materials

All chemicals and reagents used in this study were analytical-grade and used without further purification. HCl (35%),

H_2SO_4 (98%), CH_3COOH (98%), $(CH_3)_2CO$ (98%), sodium hypochlorite (NaOCl, 5.0%), absolute ethanol (99.9%), and graphite powder (≥99%) were purchased from Fine Chemicals, India. NaCl (99%), $NaNO_3$ (99%), $KMnO_4$ (99%), H_2O_2 (30%), and KOH (98%) were purchased from Loba Chemicals, India. Sodium tungstate dihydrate ($Na_2WO_4 \cdot 2H_2O$, 99%) was obtained from Alpha Chemika, India. Toluene rectified (99.9%) was purchased from Pentokey Organy, India, and polyvinyl alcohol (PVA, 99%, MW 85,000–124,000 g mol^{-1}) was obtained from Merck, India. Distilled water was used throughout the experiments.

Isolation and purification of CNFs from bamboo

The bamboo was dried in the open air, then the chopped cellulose fiber (10 g) was oven-dried and dewaxed by Soxhlet extraction with a 2 : 1 (v/v) mixture of toluene/ethanol at 70 °C for 7 h. The obtained extract was washed with distilled water and treated with NaOCl (3%) at pH 4, adjusted with glacial acetic acid (98%), while heating at 75 °C for 1 h. The bleaching process was repeated several times until the material became white, indicating the formation of holocellulose. The holocellulose was treated with 2 wt% KOH at 90 °C for 2 h to remove hemicelluloses, residual pectin, and starch. The purified cellulose powder was washed with distilled water until pH 7 and oven-dried at 105 °C to remove moisture.[22] The CNF was prepared by chemical treatment of cellulose suspension with dilute H_2SO_4 under continuous mechanical stirring (500 rpm) at 35 °C. The obtained milky suspension was centrifuged, followed by ultrasonication (SJIA-250W, Ultrasonic Homogenizer, China) to obtain well-fibrillated nano-dimensional structures. The sonication process was performed for 30 min at an output power of 400 W. The transparent supernatant obtained after centrifugation was transferred to a glass Petri dish and oven-dried at 50 °C overnight to obtain CNF (Fig. 1).[12,23]

Preparation of CNF/PVA blend

Varying concentrations of PVA solutions (0.5% and 2%) were slowly added to a previously prepared CNF dispersion (2%) while stirring at 80 °C for 2 h, followed by ultrasonication. The viscous CNF/PVA blend solution was either cast on a Petri dish
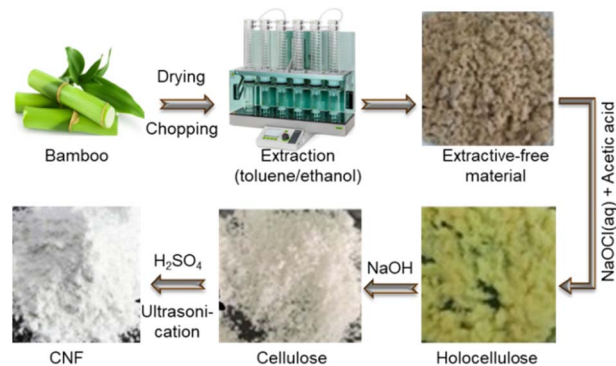

Fig. 1 Schematic of the isolation and purification of CNF from bamboo.

to form a CNF/PVA reference film or used as a blended matrix for the preparation of composite membranes.

Synthesis of graphene oxide

Graphene oxide (GO) was synthesized from graphene powder using a modification of Hummer's method.[24] Approximately 3 g of graphite powder and 1.5 g of $NaNO_3$ were added to a beaker containing 75 mL of H_2SO_4 (98%) and placed in an ice bath with continuous stirring. Subsequently, $KMnO_4$ (9 g) was gradually added, and the reaction was continued for 2 h. The solution was then removed from the ice bath and heated at 40 °C for 1 h, followed by the addition of 150 mL distilled water, and heating was continued for 1.5 h. The temperature was raised to 95 °C for 30 min then the mixture was diluted with 200 mL of distilled water under continuous stirring. H_2O_2 (30%, 30 mL) was then added to the solution while heating at 95 °C for 30 min. The mixture was then stirred for 12 h until effervescence ceased and a brilliant yellow suspension was observed. The suspension was centrifuged and the supernatant was decanted. The brown precipitates obtained were dispersed in HCl solution (10%) with vigorous stirring, followed by centrifugation. The obtained brown product was re-dispersed in distilled water, centrifuged, washed repeatedly, and dried overnight in a vacuum oven at approximately 80 °C to obtain GO.

Synthesis of rGO/WO₃ nanocomposite

A one-step *in situ* solvothermal method was used to synthesize the rGO/WO$_3$ nanocomposite.[13,14,25] In brief, the synthesized GO (0.3 g) was dispersed in distilled water (40 mL) and kept under sonication. Then, $Na_2WO_4 \cdot 2H_2O$ (7.35 g) and NaCl (1.4 g) were added to the GO dispersion while adjusting the pH to 3 with HCl (3 M). The solution was stirred using a magnetic stirrer, transferred to a 100 mL Teflon-lined stainless-steel autoclave, and kept in the hot air oven at 180 °C for 18 h for a hydrothermal reaction. The resultant residue was washed with ethanol and distilled water several times and dried at 60 °C in a vacuum oven. Similar steps were followed for the preparation of pristine rGO and WO$_3$ nanomaterials, without the addition of WO$_3$ precursors and GO, respectively.

Preparation of CNF/rGO/WO₃ membrane

An optimum CNF$_{2\%}$/PVA$_{0.5\%}$ blend solution was used as a matrix for the preparation of CNF/rGO/WO$_3$ nanocomposite membranes. Different CNF/rGO/WO$_3$ composite membranes were prepared using the solution casting method[26] by varying the weight ratio of rGO/WO$_3$ (0.5%, 1%, 3%, and 5%, m/v). The corresponding masses of rGO/WO$_3$ were then slowly added, while stirring, to a previously prepared CNF$_{2\%}$/PVA$_{0.5\%}$ dispersion. The resulting solutions were homogenized using ultrasonication, subsequently cast onto a Petri dish, and dried at room temperature for 72 h. The prepared CNF/rGO/WO$_3$ membranes were designated as CNF/rGO/WO$_3$-0.5, CNF/rGO/WO$_3$-1, CNF/rGO/WO$_3$-3, and CNF/rGO/WO$_3$-5, based on the weight ratio of rGO/WO$_3$ (0.5%, 1%, 3%, and 5%, m/v, respectively). It is noted that PVA is omitted in the final membrane designation as it acts only as a cross-linker with a low (0.5%)

concentration; thus, we choose to simplify membrane designation. The same procedures were followed to prepare CNF/rGO, CNF/WO$_3$, and CNF/PVA films.

Characterization of membrane materials

The surface morphology of nanomaterial and nanocomposite membranes was observed using a scanning electron microscope (SEM, Hitachi S-4800, USA) after carbon plating of the samples. The dimensions of CNF were determined using dynamic light scattering (DLS, V-770, JASCO International Co. Ltd, Japan). Functional group identification was achieved using a Fourier transform infrared spectrometer (FT-IR, iS50ABX Thermo-scientific, Germany). The samples were prepared and measured in a frequency range of 4000 to 400 cm^{-1}. The water contact angle of the membranes was measured using a Dataphysics OCA25 Contact Angle Measuring System (Dataphysics, Germany) by carefully dropping a 2 µL water droplet on ionogel surfaces using a syringe. The surface area was determined from the N_2 adsorption isotherms collected at 77 K using the Bru-nauer–Emmett–Teller (BET) methods (SA-9600, USA). The residual MB concentration was determined using a UV/visible spectrophotometer (V-770, JASCO International Co. Ltd, Japan).

Photocatalytic degradation study

The pollutant degradation capacity of the as-prepared photocatalytic membranes was carried out under visible light irradiation. A known amount of the prepared membranes was placed into an MB aqueous solution in a beaker and stirred for 20 min in the dark to reach the adsorption–desorption equilibrium. The mixture solution was then irradiated with an LED lamp (300 W, >380 nm). After irradiation, the concentration of MB was measured using a UV/vis spectrophotometer at its λ_{max} (664 nm) at different time intervals. The photoinduced removal efficiency (%R) and rate constant were calculated using eqn (1) and (2).[27]

$$\%R = \frac{C_0 - C}{C_0} \times 100 \tag{1}$$

$$\ln\left(\frac{C_0}{C}\right) = k_{ap}t \tag{2}$$

where; C_0 and C are the initial dye concentration and dye concentration at time t, respectively, and k_{ap} is the apparent pseudo-first-order rate constant.

Results and discussion

Dimensional analysis of CNF

The size distribution obtained from DLS for the milky white CNF suspension (0.015 %wt suspension) showed a single sharp peak with an effective hydrodynamic diameter of 38.37 nm (from 10 to 100 nm) with an observed unimodal peak. The Z average particle size was 7.513 nm, indicating the obtained cellulose suspension from acid hydrolysis of cellulose contains nanoscale particles. Similarly, Zhou *et al.* prepared a nanocellulose with a size of 115 nm from sisal fibers.[28]

Fig. 2 Schematic representation of membrane fabrication by solution casting.

Chattopadhyay and Patel isolated an approximately 348 nm CNF with a unimodal peak from rayon fibers.[29] Beyan et al. reported a cellulose fiber in the nano range (66 nm) that was isolated from enset.[30] The polydispersity index (PDI) was 0.857 (>0.1), confirming that the nanocellulose suspension had low uniformity.[23]

Optimization of membrane fabrication

The overall membrane fabrication process using solvent casting is depicted in Fig. 2. Parameters that tend to affect the morphology, integrity, and application performance of the final membranes were optimized during fabrication by varying the weight ratio of PVA and rGO/WO$_3$ fillers.

A lower concentration of PVA was assessed for its suitability for preparing a less dense CNF/PVA composite scaffold, and the corresponding effects on hydrophilicity, surface area, and porosity of the scaffold material and subsequent membranes were investigated. The average pore size, pore volume, and specific surface area of CNF/PVA, CNF/rGO/WO$_3$ (0.5% PVA), and CNF/rGO/WO$_3$ (2% PVA) membranes exhibited a typical type-I isotherm, indicating the presence of microporous structures (Table 1). With higher specific surface area and higher porosity, the CNF/rGO/WO$_3$ (0.5% PVA) was perceived to be a more suitable membrane than CNF/rGO/WO$_3$ (2% PVA), because both features can contribute to improved mass transfer and photodegradation performance. The higher surface area and porosity could be due to the lower volume proportion of PVA in the membrane. The CNF/rGO/WO$_3$ membrane with 0.5% PVA loading also exhibited a higher surface area and porosity than the CNF/PVA scaffold material. This could be due to the ability of rGO/WO$_3$ nanomaterials to act as spacers, thereby exposing the intercalated structure of CNF/rGO/WO$_3$, which is characterized by an abundance of channel structures. The introduction of rGO/WO$_3$ also prevented the folding behavior of the CNF/PVA scaffold that was observed when the film was immersed in water. The large surface areas could increase the number of active reaction sites, promoting the absorption and photodegradation of reactants.[31]
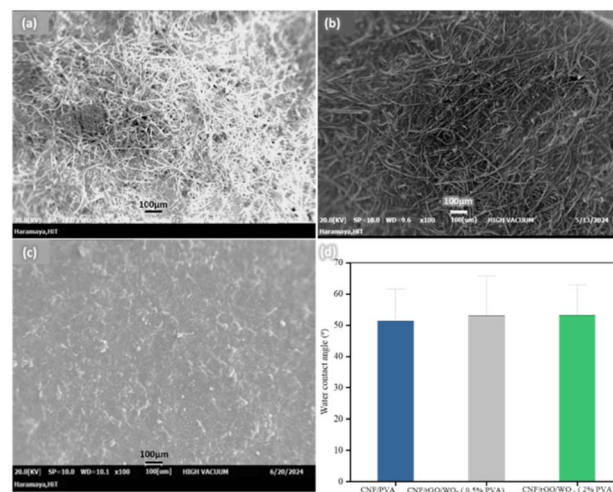

Fig. 3 SEM images of (a) CNF, (b) CNF/PVA, (c) and CNF/rGO/WO$_3$ membrane, and (d) water contact angles of the CNF/PVA, CNF/rGO/WO$_3$ (0.5% PVA), and the CNF/rGO/WO$_3$ (2% PVA) membrane.

Morphological analysis

The SEM images of CNF, CNF/PVA, and CNF/rGO/WO$_3$ are presented in Fig. 3a–c. CNF formed uniform net structures with no observable aggregates (Fig. 3a). The uniform continuous network structure was maintained after the addition of PVA (Fig. 3b), confirming the good dispersion of the CNF/PVA blend and the suitability of the film drying process. The entangled CNF network structure is still clearly visible in the denser CNF/PVA film, forming a dense and interconnected scaffold. The introduction of rGO/WO$_3$ imparts denser and more uniform membrane morphology (Fig. 3c). The progressive changes towards denser morphology while maintaining uniformity ensure the uniform distribution of rGO/WO$_3$ throughout the CNF/PVA matrix, demonstrating the successful fabrication of the CNF/rGO/WO$_3$ composite membrane, further affirming the compatibility of membrane materials. The hydrogen bonding interactions between the hydroxyl-group-rich CNF and PVA, as well as the similar interactions with rGO/WO$_3$ composite nanomaterials, could contribute to membrane integrity.[32–34] This high integrity of the constituent materials also improves membrane stability and performance.

The water contact angle (WCA) of CNF/PVA, CNF/rGO/WO$_3$ (0.5% PVA), and CNF/rGO/WO$_3$ (2% PVA) were found to be comparable, with values of 51.29°, 52.50° and 53.19°, respectively (Fig. 3d). These results indicate that the scaffold and composite membranes exhibit hydrophilic surfaces, as evidenced by their WCA of less than 90°. The hydrophilicity of the

Table 1 Specific surface area, average pore size, and average pore volume of the CNF/PVA scaffold and the CNF/rGO/WO$_3$ membranes

Membrane	Surface area (m^2 g^{-1})	Average pore size (nm)	Average pore volume (cm^3 g^{-1})
CNF/PVA (0.5% PVA)	652.9	1.278 ± 0.406	0.106 ± 0.044
CNF/rGO/WO3 (0.5% PVA)	684.3	1.294 ± 0.406	0.110 ± 0.044
CNF/rGO/WO3 (2% PVA)	669.8	1.290 ± 0.396	0.106 ± 0.044
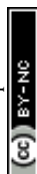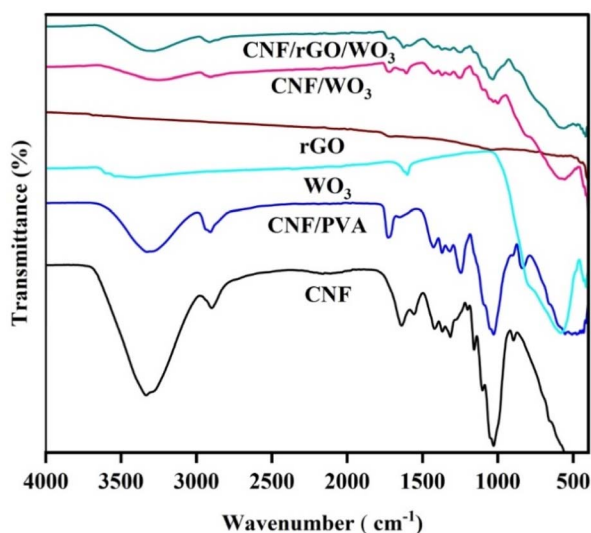
Fig. 4 FTIR spectra of the CNF, CNF/PVA, WO_3, rGO, CNF/WO_3, and the CNF/rGO/WO_3 membrane.

Fig. 5 UV/vis diffuse reflectance spectroscopy (DRS) of (a) rGO, (b) WO_3, (c) rGO/WO_3, and the (d) CNF/rGO/WO_3 photocatalytic membrane material.

CNFs and PVA is attributable to the abundance of hydroxyl functional groups, even after membrane formation, as substantiated by the FTIR results (Fig. 4).[35]

Fourier-transform infrared spectroscopy

The FTIR spectra of the WO_3, CNF, CNF/PVA, CNF/rGO, CNF/WO_3, and CNF/rGO/WO_3 membranes are shown in Fig. 4. The spectrum of the CNF/PVA film demonstrates that the peak at 3323 cm^{-1} in the CNF spectrum shifted to 3330 cm^{-1} in the spectrum of the CNF/PVA film. The peaks of pure WO_3 nanoparticles were observed at 3330, 2915, 1725, and 805 cm^{-1}. The peak centered at 805 cm^{-1} could be attributed to the stretching vibrations of W–O–W bonding.[36] A peak at 2915 cm^{-1} corresponded to C–H bonding.[37] The peaks at 1725 and 3330 cm^{-1} were assigned to the –OH bending and stretching vibrations of water molecules.[32] The peaks at around 1000–1300 cm^{-1} in CNF/rGO/WO_3, due to C–OH stretching (1060 cm^{-1}) and C–O–C bending vibrations (1243 cm^{-1}), are weakened in comparison to the peaks in CNF/PVA due to the presence of rGO and WO_3 nanoparticles.[37]

Optical properties

The UV-vis diffuse reflectance spectra of rGO, WO_3, rGO/WO_3, and CNF/rGO/WO_3 membranes are shown in Fig. 5. The edge of the absorption spectra of the rGO is red-shifted compared to that of the pristine WO_3 (Fig. 5a and b). While the pristine WO_3 exhibited a lower degree of absorption, its absorption exhibited a slight increase when WO_3 was composited with rGO in the WO_3/rGO (Fig. 5c). Furthermore, the ternary nanocomposite membrane (CNF/rGO/WO_3) absorbed light in the UV/vis region (300 to 800 nm) (Fig. 5d), which is consistent with the findings of a previous study.[38] The substantial light absorbance enhancement and shift in the visible light region of the absorption spectrum for CNF/rGO/WO_3 is primarily attributed
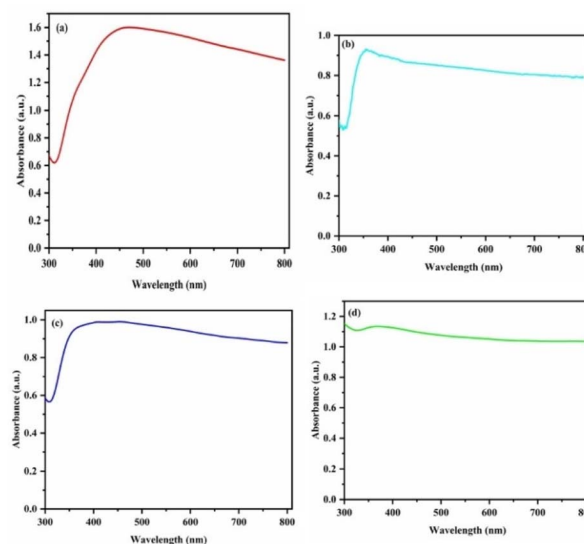
to the synergistic effect of rGO and WO_3, which facilitates light adsorption.[37]

Tauc's equation (eqn. (3)) was used to extrapolate the optical band gap of the as-prepared pristine and membrane composite photocatalyst materials.

$$(\alpha h\nu) = A(h\nu - E_g)^n; \alpha = 4\pi k/\lambda \qquad (3)$$

where α is the absorption coefficient, λ is the wavelength of the incident photon, $h\nu$ is the incident photon energy, $n = 1/2$ and 2 for direct and indirect recombination, respectively, A is an arbitrary coefficient, and E_g is the optical band gap of the material.[38]

For the indirect bandgap metal oxide semiconductor, WO_3 is presumed to have $n = 2$.[39] By extrapolating the graph of $(\alpha h\nu)^{1/2}$ vs. $h\nu$, the optical band gaps of rGO, WO_3, rGO/WO_3, and CNF/rGO/WO_3 membranes were determined to be 1.4, 2.4, 2.0, and 2.27 eV, respectively (Fig. 6a–d). The 2.27 eV band gap of the ternary nanocomposite membrane could be due to the strong absorbance of rGO over the wide UV/vis range.[38] Therefore, the CNF-based WO_3 and rGO compositing membranes reduce the optical band gap of WO_3 and enhance its photocatalytic activity.

Mechanical properties

The mechanical properties of membranes are closely related to their durability and lifespan.[40] The tensile strength and elongation at break (ε) of CNF/PVA, CNF/rGO, and CNF/WO_3 composite membranes were evaluated using a universal testing machine (UTM); the results are shown in Fig. 7. According to the data, the CNF/rGO/WO_3 composite membrane exhibited an increased tensile strength of 28.99 MPa, which is an improvement over CNF/rGO (25.9 MPa) and CNF/WO_3 (15.99 MPa), due to synergistic effects between the rigid WO_3 and rGO network. Thus, H-bonding and electrostatic interactions are favored
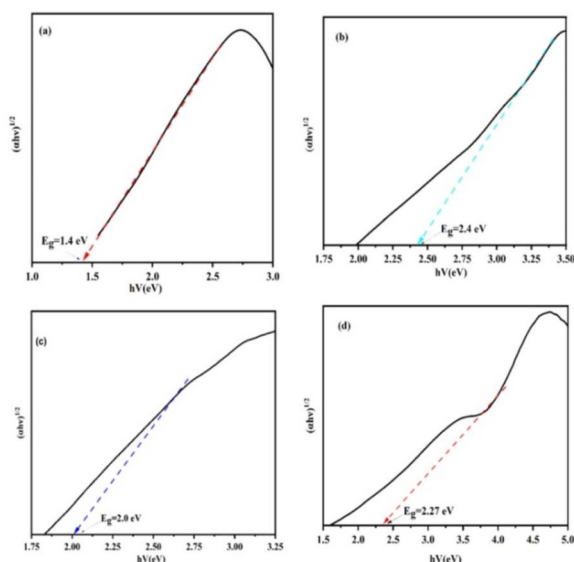
Fig. 6 Tauc plots of $(\alpha h\nu)^{1/2}$ *vs. h*ν of (a) rGO, (b) WO$_3$, (c) rGO/WO$_3$, and (d) the CNF/rGO/WO$_3$ photocatalytic membrane material.
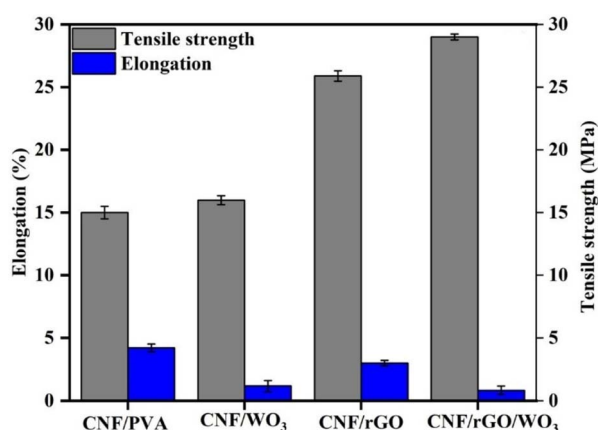

Fig. 7 Histogram showing the mechanical properties of CNF/PVA, CNF/WO$_3$, CNF/rGO, and CNF/rGO/WO$_3$ photocatalytic membrane materials.

between rGO/WO$_3$ and negatively charged CNF surfaces.[41] However, the elongation at break decreased significantly from 4.2% to 0.82%. This change could be attributed to the incorporation of the rGO/WO$_3$ composite into the CNF matrix, which significantly enhanced the mechanical strength of the membrane. The presence of photocatalytic materials likely creates an interlocking chain structure between rGO/WO$_3$ and the CNF matrix, resulting in a more compact and solid membrane structure.[17] Additionally, the membrane coated with PVA exhibited the highest tensile strength due to the cross-linking effect of PVA on the CNF-based membrane surface, further reinforcing the mechanical integrity of the membrane.

Optimization of photocatalytic degradation parameters

Effect of catalyst dosage. A series of tests were performed to investigate the effect of the rGO/WO$_3$ weight ratio in CNF/rGO/

WO$_3$-*X* on the degradation of MB. The experimental design involved the introduction of varying amounts of rGO/WO$_3$ in the 0.45 g CNF/rGO/WO$_3$-*X* (*X* = 0.5%, 1%, 3%, and 5%) while maintaining a constant MB solution concentration of 5 mg L^{-1} in a 100 mL volume. The photodegradation process was carried out under irradiation with a 300 W xenon lamp. Degradation efficiencies of 50.1%, 54.1%, 89.3%, and 69.7% were obtained with CNF/rGO/WO$_3$-0.5, CNF/rGO/WO$_3$-1, CNF/rGO/WO$_3$-3, and CNF/rGO/WO$_3$-5 membrane at 120 min, respectively (Fig. 8). As the catalyst dosage (rGO/WO$_3$) increased, the photodegradation efficiency of the CNF/rGO/WO$_3$ also improved in a certain range due to the increasing number of active sites in the catalyst (Fig. 8a). However, the CNF/rGO/WO$_3$ membrane could not use the excess active sites provided by the CNF/rGO/WO$_3$-*X* hybrid membrane at a high catalyst dose, resulting in a saturated degradation rate.[43]
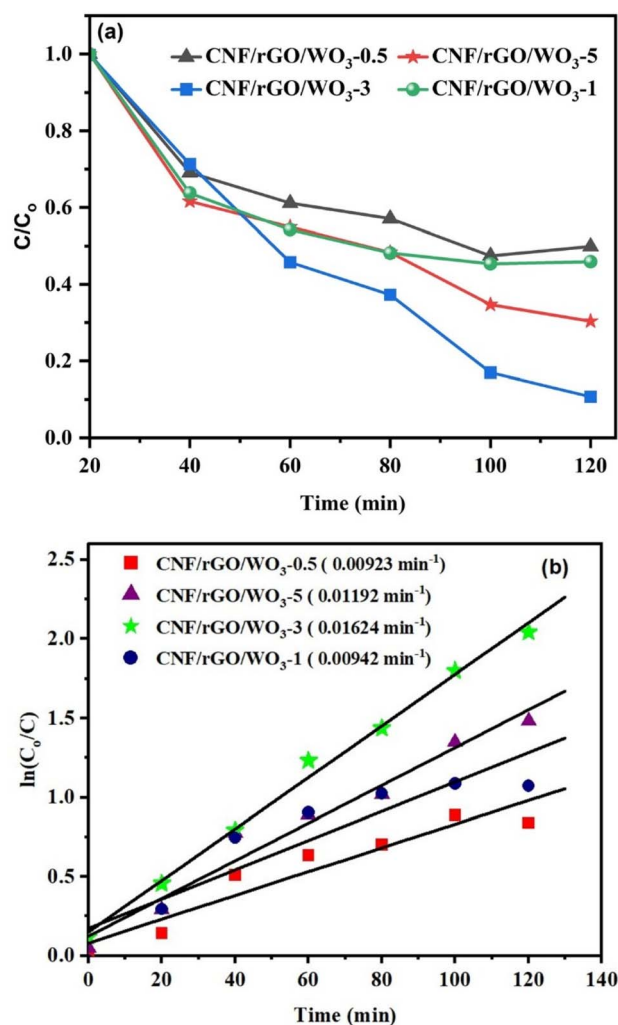

Fig. 8 (a) Plots of C/C_0 *vs.* irradiation time for photodegradation of MB in the presence of CNF/rGO/WO$_3$-0.5, CNF/rGO/WO$_3$-1, CNF/rGO/WO$_3$-3, and CNF/rGO/WO$_3$-5 membranes under visible light; and (b) photodegradation rate of MB in the presence of CNF/rGO/WO$_3$-0.5, CNF/rGO/WO$_3$-1, CNF/rGO/WO$_3$-3, and CNF/rGO/WO$_3$-5 membranes under visible light.

The surface area becomes a significant issue in the photocatalysis process because the photodegradation of an organic dye generally occurs on the photocatalyst surface. The results indicate that MB degraded more rapidly in the presence of CNF/rGO/WO$_3$-3 (89.3%) than with CNF/rGO/WO$_3$-0.5 (50.1%), CNF/rGO/WO$_3$-1 (54.1%), and CNF/rGO/WO$_3$-5 (69.7%) membranes under visible light. The optimal amount of rGO/WO$_3$ plays a significant role because rGO significantly increases the surface area and enhances the photodegradation of MB. Although CNF itself does not exhibit photocatalytic activity, its supportive role in the composite membranes is crucial in determining the overall performance. In some cases, cellulose can impede light absorption, hinder electron generation, and diminish the degradation effect of the composite.[14,19,44]

To better illustrate the degradation rates, the rate constants (k) for the degradation of MB were calculated from the well-known first-order kinetics equation $\ln(C_0/C) = kt$ (Fig. 8b). The degradation rate constant (k) was determined from the slope of the line. The CNF/rGO/WO$_3$-3 membrane (0.05195 min^{-1}) shows a higher degradation rate than CNF/rGO/WO$_3$-0.5 (0.00923 min^{-1}), CNF/rGO/WO$_3$-1 (0.00942 min^{-1}), and CNF/rGO/WO$_3$-5 (0.01192 min^{-1}) under visible irradiation, based on the result of $\ln(C_0/C)$ versus irradiation time for the photocatalytic degradation of MB.

Effect of dye concentration. The effect of dye concentration on the degradation efficiency of the photocatalytic membranes was investigated at the optimized catalyst dosage (0.45 g of CNF/rGO/WO$_3$-3) by varying the initial dye concentration (5–25 mg L^{-1}) (Fig. 9). Maximum degradation was observed at the initial dye concentration of 5 mg L^{-1} (89.3%) at 120 min. When the dye concentration was increased from 5 mg L^{-1} to 25 mg L^{-1}, the degradation efficiency of the catalyst decreased. This indicates that, as dye concentration increases, excess dye molecules can be adsorbed on the catalyst surface, thereby reducing the number of active sites of the catalysts.[45] This suggests that the system's hydroxyl radical production is insufficient for efficient dye degradation at greater concentrations, similar to previous studies.[46] Therefore, as a greater proportion of the catalyst surface

is occupied by dye molecules, fewer hydroxyl radicals can be formed and have a short lifetime to react with dye molecules. Further increases in dye concentration cause the dye molecules to be adsorbed on the photocatalyst surface and more hydroxyl radicals are required for dye molecule degradation. On the other hand, the formation of hydroxyl radicals on the catalyst surface remains constant for a given light intensity, catalyst dose, and irradiation time. Hence, the number of hydroxyl radicals are insufficient for degrading dyes at high concentrations, diminishing the photodegradation efficiency. A similar result was reported for the dyes of MB, revealing the maximum degradation at an initial dye concentration of 5 mg L^{-1}.[47]

Photocatalytic performance of the composite membrane

The photocatalytic activity of the membrane at the optimized catalyst dose and optimized initial dye concentration was
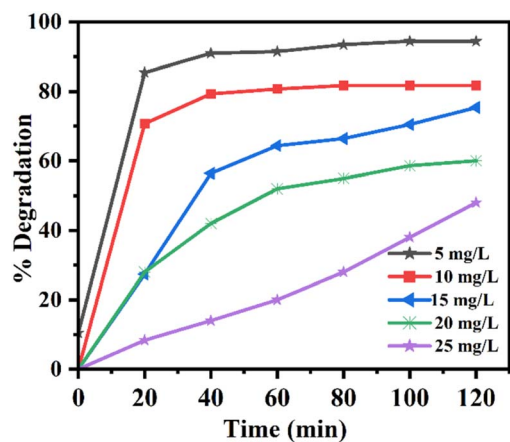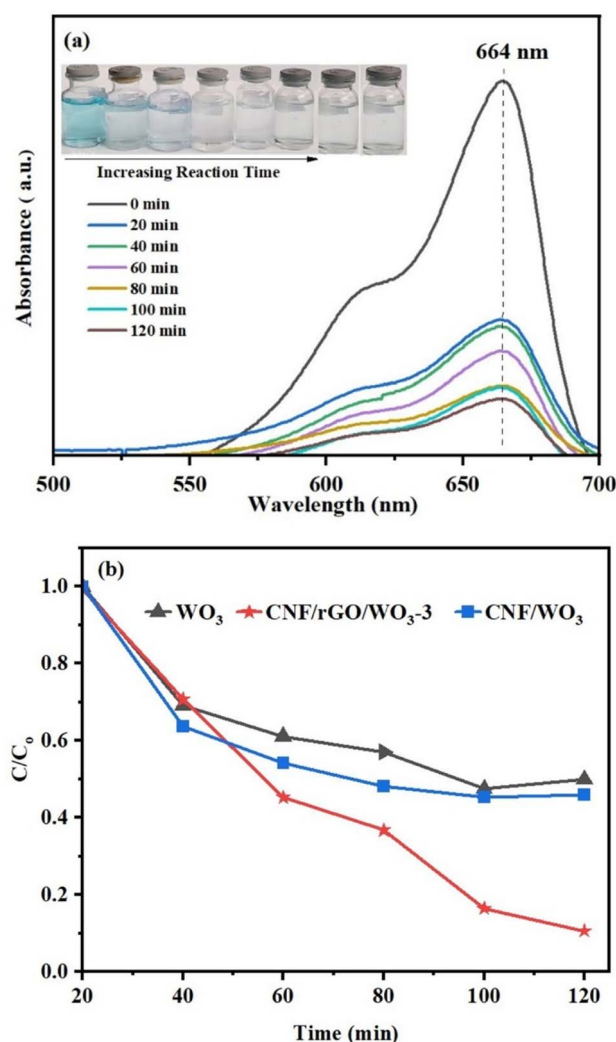

Fig. 10 (a) Photodegradation of MB by the CNF/rGO/WO$_3$-3 membrane after visible-light irradiation for 120 min (the inset shows an image of MB solutions before and after irradiation at time intervals), and (b) plots of C/C_0 vs. irradiation time for the photocatalytic degradation of MB in the presence of WO$_3$, CNF/WO$_3$, and CNF/rGO/WO$_3$-3 membranes under visible light.

Fig. 9 Effect of the initial MB dye concentration (5, 10, 15, 20, and 25 mg L^{-1}) on the photodegradation performance of the photocatalytic membranes under visible light irradiation.

evaluated by observing the degradation of MB (5 mg L^{-1}) in the presence of the CNF/rGO/WO$_3$-3 membrane (0.45 g) under visible light irradiation (Fig. 10). It can be observed that the absorbance intensity of the MB absorption peak decreased gradually. With increased irradiation time, the characteristic peak of MB absorption in the presence of CNF/rGO/WO$_3$-3 membrane was gradually reduced without shifting its optimum absorption peak position (Fig. 10a). This proved that the MB dye was completely degraded into CO$_2$ and water using the optimum catalyst dosage membrane (CNF/rGO/WO$_3$-3) without producing organic intermediates during the irradiation time.

The photocatalytic degradation MB solution at a concentration of 5 mg L^{-1} under visible light irradiation, in the presence of catalysts WO$_3$, CNF/WO$_3$, and CNF/rGO/WO$_3$ is illustrated in Fig. 10b. The enhanced photocatalytic activity of WO$_3$ nanoparticles is primarily responsible for the superior degradation observed using the CNF/rGO/WO$_3$ membranes under visible light irradiation and was evaluated using MB dye solution after 120 min of visible light exposure. Based on the C/C_0 values (Fig. 10b), pure WO$_3$ exhibited a relatively low degradation efficiency of only 50.13%, attributed to its poor light absorption activity and rapid recombination of electron–hole pairs. The binary composite CNF/WO$_3$ showed a higher degradation efficiency of 53.75%. However, under the same conditions of irradiation and time, the CNF/rGO/WO$_3$-3 membrane composite exhibited a higher degradation efficiency of 89.3%, which could be due to a greater electron acceptor ability, enhanced visible light absorption, larger surface area, and synergistic interactions among the components within the composite membrane.

Detection of reactive species

Reactive species detection tests were conducted to identify the principal active species in the photocatalytic process. Active trapping agents, including ascorbic acid (AA), isopropanol (IPA), and formic acid (FA), were utilized as superoxide radical ($^{\bullet}O_2^-$), hydroxyl radical ($^{\bullet}OH$), and hole (h$^+$) scavengers, respectively. All scavengers were employed at an equivalent concentration of 0.5 mmol L^{-1}.[48,49] The photodegradation of MB was slightly decreased with the addition of FA and IPA (Fig. 11). At 120 min reaction time, ~78.8% and ~61.74% decomposition of MB occurred in the presence of IPA and AA, respectively. However, ~89% photodegradation of MB occurred when no scavenger was present. The rate of MB degradation was significantly slower in the presence of AA, with only 47.2% of MB decomposed within 120 min. These results indicate that h$^+$ and $^{\bullet}O_2^-$, play a critical role in MB photodegradation.

$$E_{CB} = X - E - \frac{1}{2}E_g \tag{4}$$

$$E_{VB} = E_{CB} + E_g \tag{5}$$

where E_{CB} is the conduction band edge potential, E_{VB} is the valence band edge potential, and X is the absolute electronegativity of the photocatalyst (the X values of WO$_3$, rGO, rGO/WO$_3$, and CNF/rGO/WO$_3$ are 6.57 eV, 5.85 eV, 9.08 eV, and 6.05 eV, respectively[50]), E is the hydrogen scale's free electron energy (4.5
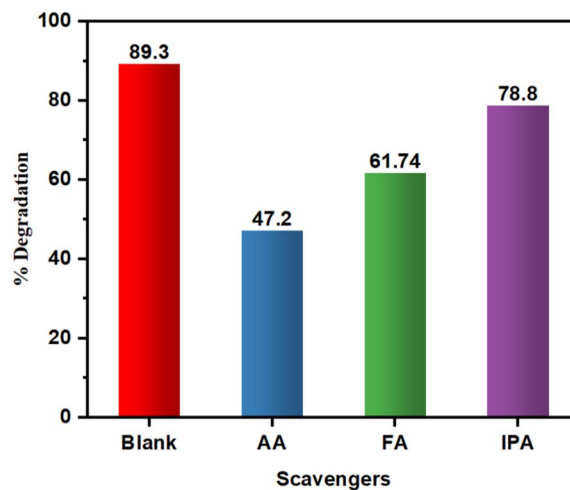

Fig. 11 Effect of different scavengers (ascorbic acid (AA), isopropanol (IPA), and formic acid (FA)) on the photodegradation reaction of MB over the CNF/rGO/WO$_3$-3 composite membrane. The E_g values for WO$_3$, rGO, rGO/WO$_3$, and CNF/rGO/WO$_3$ are 2.4, 1.4, 2.0, and 2.27 eV, respectively, and the respective E_{VB} and E_{CB} band edge positions are +3.27, +2.1, +2.15, and +2.69 eV vs. NHE and −0.87, −0.6, −0.65, and −0.42 eV vs. NHE by employing Milliken's electronegativity equations (eqn (4) and (5)).

eV), and Eg is the band-gap energy. The values of E_{VB} and E_{CB} for WO$_3$, rGO, rGO/WO$_3$, and CNF/rGO/WO$_3$ were calculated using eqn (4) and (5), respectively. The results are shown in Table 2.

The enhanced degradation of MB dye in the presence of a CNF/rGO/WO$_3$ composite membrane could be due to the delayed recombination rate of the electron (e$^-$) and holes (h$^+$) due to the electron transfer mediator nature of rGO in CNF/rGO/WO$_3$ membrane, as shown in Fig. 12. The following reactions could be suggested to occur at the interface between the prepared composite membrane and the MB dye solution.
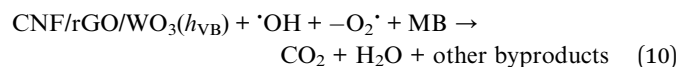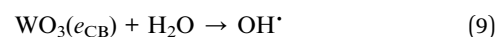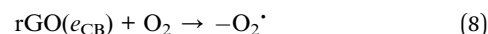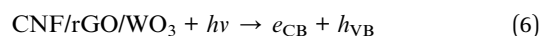
$$CNF/rGO/WO_3 + h\nu \rightarrow e_{CB} + h_{VB} \tag{6}$$

$$e_{CB} + rGO/WO_3 \rightarrow rGO(e_{CB}) \tag{7}$$

$$rGO(e_{CB}) + O_2 \rightarrow -O_2^{\bullet} \tag{8}$$

$$WO_3(e_{CB}) + H_2O \rightarrow OH^{\bullet} \tag{9}$$

$$CNF/rGO/WO_3(h_{VB}) + {}^{\bullet}OH + -O_2^{\bullet} + MB \rightarrow$$
$$CO_2 + H_2O + \text{other byproducts} \tag{10}$$
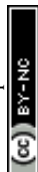
Table 2 Electronegativity (X), band gap (E_g), conduction band (E_{CB}) position and valence band (E_{VB}) of the photocatalysts on NHE

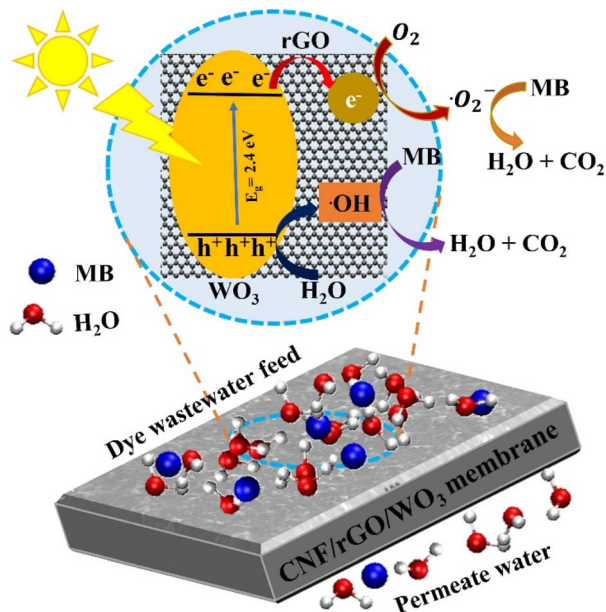| Photocatalyst	X (ev)	E_g (ev)	E_{CB} (ev)	E_{VB} (ev)
WO$_3$	6.57	2.40	0.87	3.27
rGO	5.85	1.40	0.60	2.10
rGO/WO$_3$	6.20	2.00	0.65	2.15
CNF/rGO/WO$_3$	6.05	2.27	0.42	2.69

Paper

Fig. 12 Proposed mechanism for the photodegradation of MB over the CNF/rGO/WO₃ composite membrane.

Upon exposure of the CNF/rGO/WO₃ membrane to visible light, photo-induced electrons are excited from the VB to the CB of the WO₃, generating photo-induced holes in the VB of WO₃ (eqn (6)). Then, the photoexcited electrons in the CB of the WO₃ are transferred into the rGO sheet, which leads to complete separation of the electron–hole pairs (eqn (7)). Thereafter, the transferred electrons on the surface of the rGO combine with O_2 and form $^{\cdot}O_2^{-}$ species (eqn. (8)). Furthermore, the produced $^{\cdot}O_2^{-}$ reacts with the MB pollutant, degrading it into less toxic by-products, such as CO_2 and H_2O. On the other hand; holes (h^+) in the VB of WO₃ allow H_2O_2 to react with water to produce $HO^{\cdot}$ radicals. The $HO^{\cdot}$ then mineralizes the MB dye into H_2O and CO_2 molecules (eqn (9)).[51] In summary, the rGO sheet in the composite membrane served as an electron transporter and collector by decreasing the recombination rate and increasing the photogenerated charge carrier lifetime, leading to enhanced photocatalytic performance of the CNF/rGO/WO₃ membrane (eqn. (10)).

Reusability test

The reusability of the photocatalyst membrane is another important aspect of photodegradation. The long-term stability of the CNF/rGO/WO₃ membrane was evaluated by its repeated use for the removal of MB under visible light within 120 min. At the end of each test, the samples were washed and recovered with distilled water and reused in ten cycles of photo-degradation. The recycled CNF/rGO/WO₃ photocatalyst membrane demonstrated a photodegradation efficiency for MB that was similar to the original, exhibiting a slight decrease in efficiency when utilized up to six times (Fig. 13a).

Notably, the photocatalyst membrane achieved 48% degradation of MB after ten cycles, suggesting its durability and
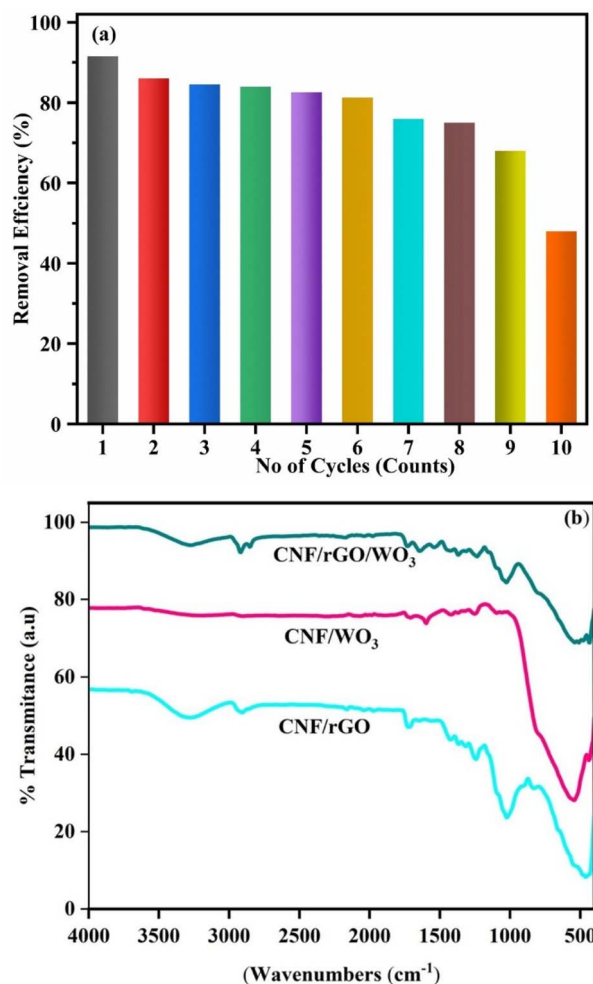

Fig. 13 (a) Reusability study of the CNF/rGO/WO₃ membrane for the degradation of MB under the optimal conditions. (b) FTIR spectra of the CNF/WO₃, CNF/rGO, and CNF/rGO/WO₃ membranes after photodegradation.

effectiveness under prolonged use. Furthermore, the molecular characteristics of the CNF/rGO/WO₃ membrane after the photocatalytic process were studied using FTIR techniques. Compared with the FTIR spectra before photodegradation (Fig. 4), the spectra after photodegradation (Fig. 13b) show some changes in peak positions and intensities, indicating surface modifications and possible fouling interactions. The O–H stretching peak becomes slightly broader and shifts to 3278.4 cm⁻¹, while the C–H stretching peak shifts to 2915 cm⁻¹. The C=O stretching peak appears at 1727 cm⁻¹ and the C–O–C stretching peak shifts to 1033.6 cm⁻¹, both with reduced intensity. These changes suggest possible adsorption of foulants on the membrane surface and minor chemical modifications during the photodegradation process. The strong W–O–W peak, which appears around 583.9 cm⁻¹ before photodegradation in the WO₃, CNF/WO₃, and CNF/rGO/WO₃ membranes, remains present after photodegradation but becomes slightly sharper. This indicates that WO₃ remains chemically stable throughout the photodegradation process, maintaining its structural integrity.[17,42]

Table 3 Comparative MB photodegradation performance of the CNF/rGO/WO$_3$ membrane with other related work

No	Membrane	Method of preparation	Weight	Target concentration (mg L^{-1})	Irradiation time	Light source	Photocatalytic degradation efficiency	Ref.
1	2D-WO$_3$/CA	Scraper method	478.13 mg	10	7 days	Sunlight	75%	52
2	CA-ZnO-NP	Spin-coating techniques	2000 mg	5	120 min	Sunlight	74%	53
3	CNF–ZnO–Ag	Drop-drying method	40 mg	10	300 min	Visible light	100%	19
4	Cellulose-TiO$_2$	Coating solution	—	5	90 min	UV irradiation	90%	54
5	WO$_{2.72}$@Fe$_3$O$_4$@CNF	Freeze-drying	—	10	120 min	Solar irradiation	85%	55
6	CNF/rGO/WO$_3$	Blend casting technique	450 mg	5	120 min	Visible light	89%	This study

The CNF/rGO/WO$_3$ membrane is effective for the photodegradation of MB. Its characteristics, including preparation method, irradiation time, target concentration, weight dose, and photocatalytic degradation efficiency are compared to those reported in other studies in Table 3. The CNF/rGO/WO$_3$ membrane is prepared using the solution casting method, which is similar to the blend casting techniques used for the membrane preparation. Various studies reported irradiation times ranging from a maximum of 7 days to a minimum of 90 min. Our results demonstrate a significant photodegradation efficiency of 89.3% at 120 min irradiation under visible light, which is comparable to the time needed for the complete degradation of various molecules under similar conditions, demonstrating the excellent photocatalytic reactivity of the system with organic pollutants. Notably, while the highest photodegradation reported was 100% for the CNF–ZnO–Ag membrane, that system required 300 min of irradiation time. This underlines the efficiency of the current study in achieving effective MB degradation within a shorter irradiation time.

Conclusion

The environmentally friendly ternary composite CNF/rGO/WO$_3$ nanocomposite membrane was prepared using the blend solution casting technique. The structural properties of the nanostructures and the membranes were investigated. The morphological results showed that the rGO/WO$_3$ nanoparticles could be uniformly distributed along the CNF/PVA with heating, increasing the surface area, the mechanical properties of the membrane, and the number of active sites available for the removal of dye molecules. The CNF/rGO/WO$_3$ membrane can effectively stimulate the separation of electron–hole pairs generated by rGO/WO$_3$ in the nanocomposite and enhance the photocatalytic capacities of the CNF-based membrane under visible-light irradiation. The CNF/rGO/WO$_3$ composite membrane exhibits a higher photodegradation capacity than pure WO$_3$ MB at 120 min. The design provides a green approach with excellent photodegradation performance for the remediation of organic pollutants, and can enable further applications for photocatalysis and wastewater treatment. Compared with WO$_3$ and CNF/WO$_3$, the CNF/rGO/WO$_3$ membrane exhibits faster photocatalytic degradation rates and efficient reusability. The CNF-supported photocatalytic membrane features a simple design that is economical, requires low energy consumption, and is environmentally friendly.

Data availability

The data supporting this article have been included as part of the ESI.†

Author contributions

MTY: investigation, material preparation, and writing original draft; GG: conceptualization, supervision, methodology, writing: review and editing; AKM: conceptualization, supervision, methodology, writing: review and editing; KNM:

conceptualization, supervision, methodology, writing: review and editing.

Conflicts of interest

There are no conflicts to declare.

Acknowledgements

References

1 K. K. Ibraheem, O. Y. T. Al-Janabi, E. T. B. Al-Tikrity, I. S. Ali, B. M. Ahmed and P. J. S. Foot, *Inorg. Chem. Commun.*, 2025, **173**, 113844.

2 M. T. Yifira, A. K. Mersha, G. Gebreslassie and K. N. Mekonnen, *Carbohydr. Polym. Technol. Appl.*, 2024, **8**, 100589.

3 D. Singh, F. Khan, V. K. Jain and S. Bhattacharya, *J. Indian Chem. Soc.*, 2024, **101**, 101356.

4 H. Fan, Y. Quan, X. Zhao, H. Chen, S. Yu, Q. Zhang and Y. Zhang, *J. Appl. Polym. Sci.*, 2017, **134**, 1–9.

5 Y. Ibrahim, E. Abdulkarem, V. Naddeo, F. Banat and S. W. Hasan, *Sci. Total Environ.*, 2019, **690**, 167–180.

6 C. Vilela, C. Moreirinha, A. Almeida, A. J. D. Silvestre and C. S. R. Freire, *Materials*, 2019, **12**, 1404.

7 W. Wang, Q. Bai, T. Liang, H. Bai and X. Liu, *Polymers*, 2017, **9**, 455.

8 C. Zhu, P. Liu and A. P. Mathew, *ACS Appl. Mater. Interfaces*, 2017, **9**, 21048–21058.

9 G. Huang, D. Zeng, M. Wei, Y. Chen and A. Ma, *Inorg. Chem. Commun.*, 2025, **172**, 1–10.

10 B. Parasuraman, B. Kandasamy, V. Vasudevan and P. Thangavelu, *Environ. Sci. Pollut. Res.*, 2024, **31**, 46591–46601.

11 A. T. Sheikhzadeh and A. Mouradzadegun, *Photochem. Photobiol. Sci.*, 2023, **22**, 837–855.

12 C. Yadav, A. Saini and P. K. Maji, *Carbohydr. Polym.*, 2017, **165**, 276–284.

13 V. Ramar and K. Balasubramanian, *ACS Appl. Nano Mater.*, 2021, **4**, 5512–5521.

14 S. S. Mehta, D. Y. Nadargi, M. S. Tamboli, T. Alshahrani, V. R. M Reddy, E. S. Kim, I. S. Mulla, C. Park and S. S. Suryavanshi, *Sci. Rep.*, 2021, **11**, 1–17.

15 W. Zhu, F. Sun, R. Goei and Y. Zhou, *Appl. Catal. B Environ.*, 2017, **207**, 93–102.

16 K. Dhivyaprasath, B. R. Wiston, M. Preetham, S. Harinee and M. Ashok, *Optik*, 2021, **244**, 167593.

17 T. D. Kusworo, M. Yulfarida, A. C. Kumoro, S. Sumardiono, M. Djaeni, T. A. Kurniawan, M. H. D. Othman and B. Budiyono, *J. Environ. Chem. Eng.*, 2023, **11**, 109583.

18 F. Dai, S. Zhang, Q. Wang, H. Chen, C. Chen, G. Qian and Y. Yu, *Front. Chem.*, 2021, **9**, 1–13.

19 J. Han, N. B. Tri Pham, K. Oh and H. K. Choi, *ACS Omega*, 2024, **9**, 7143–7153.

20 T. A. Hameed, A. Salama and R. A. Nasr, *J. Polym. Environ.*, 2024, **32**, 4440–4455.

21 L. A. Worku, R. K. Bachheti and M. G. Tadesse, *Int. J. Polym. Sci.*, 2022, **1**, 155552.

22 Y. Hu, L. Tang, Q. Lu, S. Wang, X. Chen and B. Huang, *Cellulose*, 2014, **21**, 1611–1618.

23 E. G. Bacha and H. D. Demsash, *Extraction and Characterization of Nanocellulose from Eragrostis Teff Straw*, 2021, Preprint (Version 1), available at Research Square, DOI: **10.21203/rs.3.rs-296990/v1**.

24 L. Shahriary and A. A. Athawale, *Int. J. Renew. Energy Environ. Eng.*, 2014, **02**, 58–63.

25 V. Ramar and K. Balasubramanian, *Appl. Phys. A Mater. Sci. Process.*, 2018, **124**, 1–11.

26 U. Siemann, *Prog. Colloid Polym. Sci.*, 2005, **130**, 1–14.

27 Z. Yina, Z. Li, Y. Deng, M. Xueb, Y. Chen, J. Ou, Y. Xie, Y. Luo, C. Xie and Z. Hong, *Ind. Crops Prod.*, 2023, **197**, 116672.

28 Y. M. Zhou, S. Y. Fu, L. M. Zheng and H. Y. Zhan, *Express Polym. Lett.*, 2012, **6**, 794–804.

29 D. P. Chattopadhyay and B. H. Patel, *J. Text. Sci. Eng.*, 2016, **6**(2), 1–8.

30 S. M. Beyan, T. A. Amibo, S. V. Prabhu and A. G. Ayalew, *J. Nanomater.*, 2021, 7492532.

31 C. Zhao, F. Ran, L. Dai, C. Li, C. Zheng and C. Si, *Carbohydr. Polym.*, 2021, 117343.

32 M. Kaur, S. Singh, S. K. Mehta and S. K. Kansal, *Molecules*, 2022, **27**, 6956.

33 M. Wohlert, T. Benselfelt, L. Wågberg, I. Furó, L. A. Berglund and J. Wohlert, *Cellulose*, 2022, **29**, 1–23.

34 P. Song, Z. Xu, Y. Lu and Q. Guo, *Macromolecules*, 2015, **48**, 3957–3964.

35 A. Autissier, C. Le Visage, C. Pouzet, F. Chaubet and D. Letourneur, *Acta Biomater.*, 2010, **6**, 3640–3648.

36 L. Tie, C. Yu, Y. Zhao, H. Chen, S. Yang, J. Sun, S. Dong and J. Sun, *J. Alloys Compd.*, 2018, **769**, 83–91.

37 L. Yang, C. Chen, Y. Hu, F. Wei, J. Cui, Y. Zhao, X. Xu, X. Chen and D. Sun, *J. Colloid Interface Sci.*, 2020, **562**, 21–28.

38 V. A. Tran, T. P. Nguyen, V. T. Le, I. T. Kim, S.-W. Lee and C. T. Nguyen, *J. Sci. Adv. Mater. Devices*, 2021, **6**, 108–117.

39 C. T. Nguyen, T. P. Pham, T. L. A. Luu, X. S. Nguyen, T. T. Nguyen, H. L. Nguyen and D. C. Nguyen, *Ceram. Int.*, 2020, **46**, 8711–8718.

40 Y. Zhang, Q. Zhang, Y. Li and L. Chen, *Struct. Eng. Mech.*, 2014, **49**(6), 745–762.

41 K. Fernández, A. Llanquileo, M. Bustos, V. Aedo, I. Ruiz, S. Carrasco, M. Tapia, M. Pereira, M. F. Meléndrez, C. Aguayo and L. I. Atanase, *Polymers*, 2023, **15**(12), 2752.

42 I. Koyuncu, B. Eryildiz, R. Kaya, Y. Karakus, F. Zakeri, A. Khataee and V. Vatanpour, *J. Environ. Manage.*, 2023, **326**, 116758.

43 W. Zhu, M. Han, D. Kim, J. Park, H. Choi, G. Kwon, J. You, S. Li, T. Park and J. Kim, *J. Water Process Eng.*, 2023, **53**, 103620.

44 S. Elbakry, M. E. A. Ali, M. Abouelfadl, N. A. Badway and K. M. M. Salam, *J. Photochem. Photobiol., A*, 2022, **430**, 113957.

45 I. K. Konstantinou and T. A. Albanis, *Appl. Catal., B*, 2004, **49**, 1–14.

46 P. V. Nidheesh and R. Rajan, *RSC Adv.*, 2016, **6**, 5330–5340.

47 S. D. Khairnar, M. R. Patil and V. S. Shrivastava, *Iran. J. Catal.*, 2018, **8**, 143–150.

48 G. Gebreslassie, M. Gebrezgiabher, B. Lin, M. Thomas and W. Linert, *Inorganics*, 2023, **11**(3), 119.

49 H. D. Weldekirstos, T. Mengist, N. Belachew and M. L. Mekonnen, *Results Chem.*, 2024, **7**, 101306.

50 A. Sarkar, A. Mandal, S. Mandal, S. K. Sen, D. Banerjee, S. Ganguly and K. Kargupta, *J. Chem. Sci.*, 2024, **136**(2), 1–11.

51 H. A. Alburaih, M. Aadil, S. Mubeen, W. Hassan, S. R. Ejaz, A. Anwar, S. Aman and I. A. Alsafari, *FlatChem*, 2022, **34**, 100380.

52 B. Qi, T. Chen, Z. Liu, J. Qi, Q. Wang, W. Zhang and X. Li, *J. Water Process Eng.*, 2022, **47**, 102739.

53 M. A. Abu-Dalo, S. A. Al-Rosan and B. A. Albiss, *Polymers*, 2021, **13**(19), 3451.

54 H. K. M. Ng and C. P. Leo, *Prog. Org. Coat.*, 2019, **132**, 70–75.

55 S. Chaudhuri, C. M. Wu and K. G. Motora, *J. Photochem. Photobiol., A*, 2023, **438**, 114525.